Quantitative evaluation of the lunar seismic scattering and comparison between the Earth, Mars, and the Moon

K. Onodera[1,2,3], T. Kawamura[2], S. Tanaka[4], Y. Ishihara[5], T. Maeda[6]

[1]Earthquake Research Institute, The University of Tokyo, Tokyo, Japan.

[2]Université Paris Cité, Institut de Physique du Globe de Paris, CNRS, Paris, France.

[3]The Graduate University for Advanced Studies, SOKENDAI, Kanagawa, Japan.

[4]Institute of Space and Astronautical Sciences, Japan Aerospace Exploration Agency, Kanagawa, Japan.

[5]JAXA Space Exploration Center (JSEC), Japan Aerospace Exploration Agency, Kanagawa, Japan.

[6]Graduate School of Science and Technology, Hirosaki University, Aomori, Japan.

Contents of this file

Text S1 to S4
Figures S1 to S4
Tables S1 to S7

Introduction

This document includes the supplementary information about the detailed configuration of numerical simulations, the topography models, and the parameter studies concerning correlation length. Also, some figures and tables are included in to help readers better understand the contents of the main text.

Supporting Texts

Text S1. Configuration for numerical simulations

To realize a stable wave-propagation simulation up to 2.0 Hz, the parameters are optimized using a tool provided in the OpenSWPC (called "fdmcond.x"). It returns us the reasonable parameters for a computation we want to perform by evaluating the "wavelength condition" and "stability condition" (Maeda et al., 2017). The wavelength condition is related to the spatial resolutions (d_x, d_y, d_z), requiring that the grid number is at least $5 - 10$ for a wavelength. The stability condition is related to both spatial and temporal resolution. In N_D-dimensional space for the p-order finite difference method, the condition is defined as:

$$dt \leq \frac{\left(\sum_{p=1}^{P/2} C_p\right)^{-1}}{V_{max}} \left(\sum_{i=1}^{N_D} \frac{1}{d_{x_i}^2}\right)^{-1/2} \quad (S1)$$

where V_{max} is the maximum velocity within a medium, C_p is the coefficient of the finite difference formula ($C_1 = 9/8$ and $C_2 = 1/24$ for 4th order accuracy in space as in this study), and d_{x_i} is the spatial resolution (or spatial grid width) in i-th direction. The parameters for the numerical simulations are summarized in Table S4, and the corresponding workspaces are visualized in Figure 2 in the main text.

Text S2. Determination of ξ value

In order to determine the empirical constant ξ in Equation 4 in the main text, we computed the travel time for the two target artificial impacts. One is Apollo 16 SIVB impact recorded at Station 12 and the other is Apollo 14 SIVB impact observed at Station 12 (Figure 2 in the main text). The epicentral distances are 153.76 km and 175.34 km, respectively. Let us consider a stratified half-space where L is the epicentral distance, H_i and v_i represent the layer thickness and P-wave velocity at the i-th layer, respectively. θ_i is a critical angle at the i-th layer. According to Snell's law, $\theta_i = \arcsin(v_i/v_{i+1})$. In the case of the direct wave, the travel time t_{dir} can be computed as:

$$t_{dir} = L/v_i \quad (S2)$$

The travel time for refracted wave (t_{ref}) can be estimated considering the shortest path from the seismic source to the station through the underground. When $L > \sum_{i=1}^{N} 2H_i tan\theta_i$, t_{ref} can be expressed using the critical angles at respective boundaries like:

$$t_{ref} = 2\left[\sum_{i=1}^{N} \frac{H_i}{v_i cos\theta_i} + \left(\frac{L}{2} - \sum_{i=1}^{N} H_i tan\theta_i\right)/v_{i+1}\right] \quad (S3)$$

60   As $cos\theta_i = (1 - v^2_i / v^2_{i+1})^{1/2}$ and $tan\theta_i = v_i (v^2_{i+1} - v^2_i)^{-1/2}$, Equation S3 becomes

61
$$t_{ref} = 2\left[\sum_{i=1}^{N} \frac{H_i}{v_i\sqrt{1-(v_i/v_{i+1})^2}} + \left(\frac{L}{2} - \sum_{i=1}^{N} \frac{H_i}{\sqrt{v_{i+1}^2 + v_i^2}}\right)/v_{i+1}\right] \quad (S4)$$

62   Travel times for several structure models shown in Figure S1 were computed using Equation S2 or

63   S4. Figure S2 displays the computed travel times for various structure models ($\xi = 2.0 - 24$). The

64   dotted lines show the estimated range of travel times for respective artificial impacts by Lognonné

65   et al. (2003). Note that while the reading error of P-wave arrival is about 1 s for both events, Apollo

66   16 SIVB impact includes an extra error in origin time by at least 4 s due to the loss of radio-tracking

67   during the operation (Toksöz et al., 1974). Since $\xi=7$ explains the travel times for both impacts, we

68   constructed a reference velocity structure based on that ξ parameter.

69

70   **Text S3. Topography model**

71   For the surface topography model, we employed one of the highest-resolution lunar digital

72   elevation models (DEMs) available today. It is called "SLDEM2015 (Barker et al., 2016)", which was

73   constructed based on the Lunar Orbiter Laser Altimeter (LOLA) data by Lunar Reconnaissance Orbiter

74   (LRO) combined with the DEM produced by Terrain Camera (TC) onboard SELENE (Kaguya). This

75   model covers from ± 60 degrees in latitude and ± 180 degrees in longitude with the highest horizontal

76   spatial resolution being 59 m. The original data are available on NASA Planetary Data System (PDS).

77   Concerning the crust-mantle boundary and/or Moho boundary, the crustal structure models

78   (GL0420A) provided by Wieczorek et al. (2013) were utilized. Their models were constructed from the

79   observation of gravity anomalies by the GRAIL mission. Particularly, in order to make it consistent

80   with a density model shown before, we adopted Model 2 which was made with a combination of the

81   GRAIL observation and the crustal thickness (30.8 km at the Apollo 12/14 landing site) estimated from

82   the travel-time analysis using the Apollo seismic data by Lognonné et al.(2003). As the crustal model

83   truncates the degree higher than 310, it provides us the spatial resolution of 0.43 degrees. The original

84   dataset was downloaded from GRAIL Crustal Thickness Archive (Wieczorek et al., 2013).

85   In addition to the surface and Moho topographies, we also assumed some layers to express the

86   gradual change in the seismic velocity profile with depth. Since the seismic velocity changes rapidly

87   near-surface, we prepared a more densely layered structure at the first 5 km compared to the deeper

88   parts. Following Onodera et al. (2021), the respective boundary depths are defined as:

89
$$D_i(\theta, \phi) = D_s(\theta, \phi) + \frac{D_M(\theta,\phi) - D_s(\theta,\phi)}{c_i} \quad (S5)$$

90   where $D_i(\theta, \phi)$ is the boundary depth of i-th layer at the coordinates of longitude θ and latitude ϕ, and

91   D_s and D_M are the surface elevation from the mean radius of the Moon (1737.4 km) and the Moho

92   boundary depth, respectively. C_i is a constant to make the mean boundary at the target region (Figure

93   S3) consistent with i-th layer's depth (Table S5). Note that the surface DEM was downsampled to make

94   the spatial resolution match that of Moho boundary model. This kind of procedure makes the deeper

95   structure reflect the Moho undulations and the shallower reflect the surface topographical variations.

96

97   **Text S4. Parameter study of the correlation length**

98   The simulation results for three correlation-length cases are compared here ($a = 0.20, 0.65, 2.0$)

99   (Figure S4). In the case of $a = 0.20$, the envelope looks relatively well fitted with the data, although

100 its spectrogram indicates the surface wave energy is not completely scattered. Compared with the

101 spectrogram of $a = 0.65$, it is considered that the correlation length of 0.20 km is not large enough

102 to influence the lower frequency components. On the other hand, $a = 2.0$ shows a strong peak

103 around 140 s in the envelope, which can also be seen as the concentration of energy around 1 Hz

104 in the spectrogram. Therefore, this random medium does not appear suitable for the Apollo 12

105 landing site.

106

107

108

109

110

111

112

113

114

115

116

117

118

119

120

121

122

123

124

125

Supp
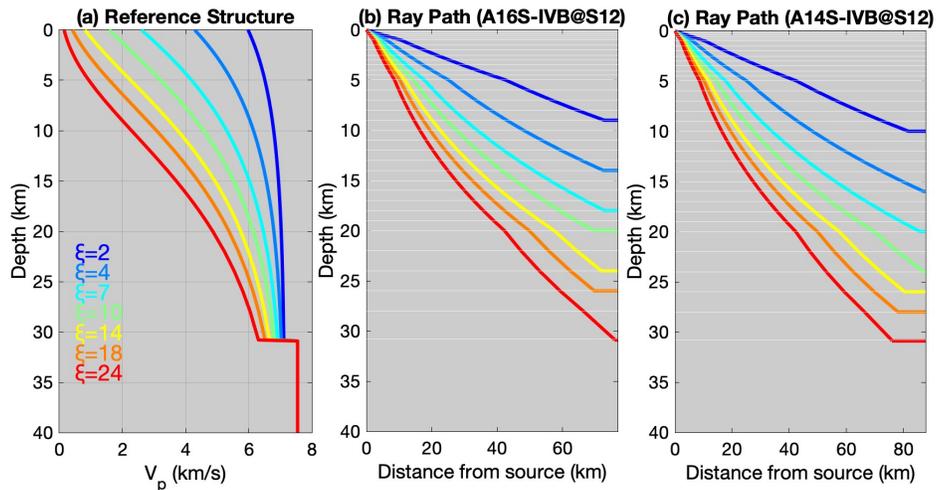
Figure S1. (a) Reference P-wave velocity models based on Equation 4 in Methods (ξ=2, 4, 7, 10, 14, 18, 24). The velocity jump at 30.8 km corresponds to the Moho boundary at the Apollo 12 landing site. P-wave velocity below 30.8 km is from VPREMoon by Garcia et al. (2011). (b) Ray path for each velocity model for Apollo 16 SIVB at Station 12 case. (c) Ray path for each velocity model for Apollo 14 SIVB at Station 12 case. The horizontal axis corresponds to the distance ranging from the source to the halfway through the station.
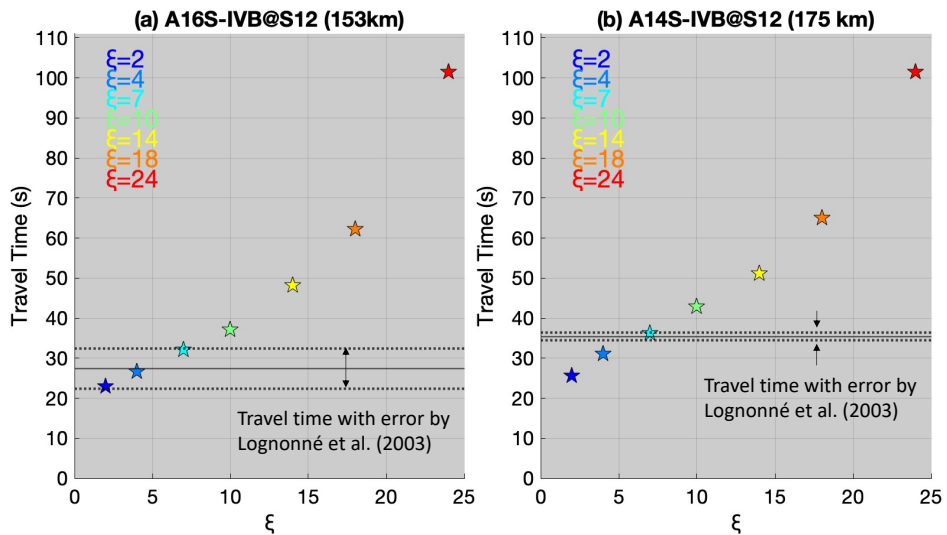

Figure S2.

16 SIVB at

at Station 1~~2 case with the epicentral distance of 175±4 km. The dotted lines show the error~~ range of the travel time determined by Lognonné et al. (2003). The uncertainty of P-wave arrival is 1 s. Note that Apollo 16 SIVB has an additional 4 s error in origin time due to the loss of radio-tracking during its operation (Toksöz et al., 1974).

141
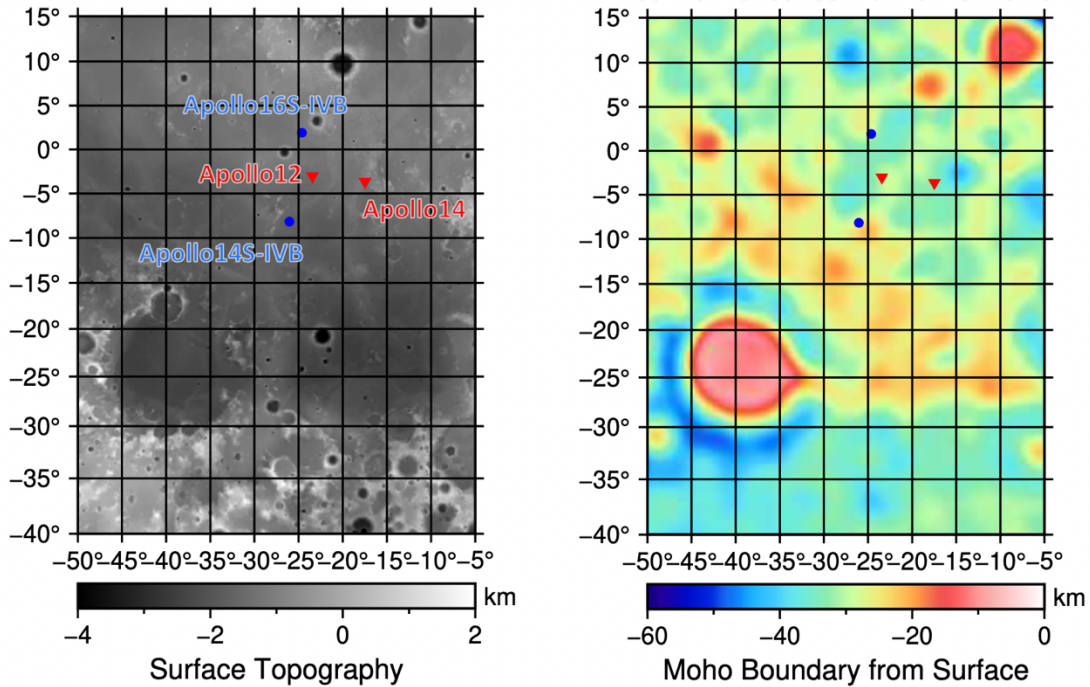
Figure S3. Target region shown as surface topography map (left) and Moho boundary depth (right). Red plots show the locations of the Apollo seismic stations and blue ones show the impacts of Apollo SIVB rocket boosters used in this study.
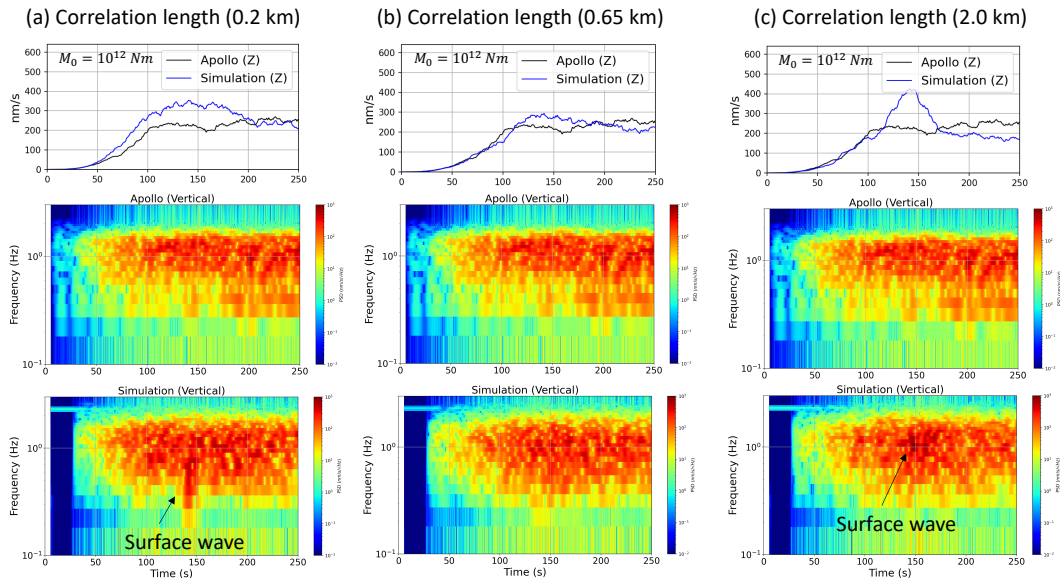
145
146 **Figure S4. Comparison of synthetics with different correlation length (a: 0.2 km, b: 0.65 km, c: 2.0 km). The top row shows the smoothed envelopes for the vertical component. The black envelopes are for the Apollo data (Apollo 16 SIVB impact), and the blue ones are for the respective simulation cases. The second row displays the spectrogram for the Apollo, and the third row is the spectrogram for the simulation outputs.**

6

Supporting tables

**Table S1. Intrinsic Q structure for P- and S-waves assumed in this study.**

Layer	^PQ_i	^SQ_i	Reference
0 – 10 km	6750	6750	Nakamura and Koyama (1982)
10 – 20 km	5000	5000	Blanchette-Guertin et al. (2012)
20 – 30 km	4000	4000	Blanchette-Guertin et al. (2012)
> 30 km	3750	1500	Nakamura and Koyama (1982)

Table S2. List of general information of Apollo artificial impacts by Toksöz et al. (1974).[*]These parameters are estimated based on the improved impact location for Apollo16 S-IVB by Wagner et al. (2017).

Impactor	Date	Times received on Earth (UT)	Impact velocity (km/s)	Impact energy (J)
Apollo 12 LM	Nov-20-1969	22h17m17.7s	1.68	3.36×10^9
Apollo 14 LM	Feb-7-1971	00h45m25.7s	1.68	3.25×10^9
Apollo 15 LM	Aug-3-1971	03h03m37.0s	1.70	3.44×10^9
Apollo 17 LM	Dec-15-1972	06h50m20.8s	1.67	3.15×10^9
Apollo 13 SIVB	Apr-15-1970	01h09m41.0s	2.58	4.63×10^{10}
Apollo 14 SIVB	Feb-4-1971	07h40m55.4s	2.54	4.52×10^{10}
Apollo 15 SIVB	Jul-29-1971	20h58m42.9s	2.58	4.61×10^{10}
Apollo 16 SIVB	Apr-19-1972	21h02m4s±4s	2.5-2.6*	4.59×10^{10}
Apollo 17 SIVB	Dec-10-1972	20h32m42.3s	2.55	4.71×10^{10}

Table S3. List of impact locations and angles of Apollo artificial impacts. Impact locations of Lunar Modules (LMs) are referred from Toksöz et al. (1974) and those of S-IVB impacts are referred from Wagner et al. (2017). Impact angles and Heading angles are referenced from Orloff (2000).

Impactor	Latitude (°N)	Longitude (°E)	Angle from horizon (°)	Heading angle (N°E)
Apollo 12 LM	-3.94	338.80	3.7	305.85
Apollo 14 LM	-3.42	340.33	3.6	282
Apollo 15 LM	26.36	0.25	3.2	284
Apollo 16 LM	19.96	30.50	-	-
Apollo 13 SIVB	-2.5550	332.1125	76	259.4
Apollo 14 SIVB	-8.1810	333.9695	69	284.3
Apollo 15 SIVB	-1.2897	348.1755	62	276.54
Apollo 16 SIVB	1.9210	335.3770	79	255.3
Apollo 17 SIVB	-4.1681	347.6693	55	277

169 **Table S4. List of parameters. Note that the coordinate system follows that of the OpenSWPC (i.e.,**
170 **+x is north, +y is east, +z points downward). Values in parentheses are for Apollo 16 SIVB impact**
171 **while values without parentheses are for Apollo 14 SIVB impact.**

Parameter name	Symbol	Value
Spatial resolution (km)	d_x	3.5×10^{-2}
	d_y	3.5×10^{-2}
	d_z	3.0×10^{-2}
Time resolution (s)	dt	2.15×10^{-3}
Grid number	N_x	10,500
	N_y	10,500
	N_z	1,350
Time step	N_t	170,000
Corresponding regional space (km)	L_x	367.5
	L_y	367.5
	L_z	40.5
Coordinates at origin (°)	c_{lon}	$-26.0305 \ (-24.623)$
	c_{lat}	$-8.181 \ (1.921)$
Coordinates at the lower left corner in Cartesian (km)	x_{beg}	$-140 \ (-240)$
	y_{beg}	$-150 \ (-140)$
Beginning of the vertical plane (km)	z_{beg}	-1.5

172
173
174 **Table S5. List of assumed boundaries within the lunar crust. C_i is obtained by dividing the average**
175 **crustal thickness (28.59 km) at the target region (40°S/15°N/50°W/5°W) with i-th boundary depth.**

i-th layer	Mean boundary depth (km)	C_i value	i-th layer	Mean boundary depth (km)	C_i value
1	0.2	142.94	17	9.0	3.176
2	0.4	71.47	18	10	2.859
3	0.6	47.65	19	11	2.599
4	0.8	35.74	20	12	2.382
5	1.0	29.59	21	13	2.199
6	1.5	19.06	22	14	2.042
7	2.0	14.29	23	15	1.906
8	2.5	11.44	24	16	1.787
9	3.0	9.529	25	17	1.682
10	3.5	8.168	26	18	1.588
11	4.0	7.147	27	19	1.505
12	4.5	6.353	28	20	1.429
13	5.0	5.718	29	22	1.299
14	6.0	4.765	30	24	1.191
15	7.0	4.084	31	26	1.100
16	8.0	3.574	32	28	1.021

176
177
178
179
180
181
182
183
184
185

186 **Table S6. References used in Figure 11a in the main text**

Number	Place	Reference
1	Kanto-Tokai, Japan	Fehler et al. (1992)
2	Long Valley, California	Mayeda et al. (1992)
3	Central California	
4	Hawaii	
5	Average in Japan	Hoshiba (1993)
6	Southern California	Jin et al. (1994)
7	Southern California	Leary and Abercrombie (1994)
8	Northern Greece	Hatzidimitriou (1994)
9	Southern Spain	Akinci et al. (1995)
10	Southern California	Adams and Abercrombie (1998)
11	Northeastern Venezuela	Ugalde et al. (1998)
12	Eastern Turkey	Akinci and Eyidogan (2000)
13	Southern Apennines, Italy	Bianco et al. (2002)
14	South Central Alaska	Dutta et al. (2004)
15	Southern Netherlands	Goutbeek et al. (2004)
16	Northeastern Colombia	Vargas et al. (2004)
17	Northeastern Italy	Bianco et al. (2005)
18	Southern Sicily, Italy	Giampiccolo et al. (2006)
19	Asama volcano, Japan	Yamamoto and Sato (2010)
20	Lithosphere and upper mantle	Lee et al. (2003), Lee et al. (2006)
21	Lower mantle (> 670 km depth)	Lee et al. (2003), Lee et al. (2006)
22	Mars	Menina et al. (2021)
23	Lunar crust	Gillet et al. (2017)
24	Lunar megaregolith	This study

187 **Table S7. References used in Figure 11b in the main text.**

Number	Place	Reference
1	Kanto-Tokai, Japan	Fehler et al. (1992)
2	Long Valley, California	Mayeda et al. (1992)
3	Central California	
4	Hawaii	
5	Average in Japan	Hoshiba (1993)
6	Southern California	Jin et al. (1994)
7	Southern California	Leary and Abercrombie (1994)
8	Northern Greece	Hatzidimitriou (1994)
9	Southern Spain	Akinci et al. (1995)
10	Southern California	Adams and Abercrombie (1998)
11	Northeastern Venezuela	Ugalde et al. (1998)
12	Eastern Turkey	Akinci and Eyidogan (2000)
13	Southern Apennines, Italy	Bianco et al. (2002)
14	South Central Alaska	Dutta et al. (2004)
15	Southern Netherlands	Goutbeek et al. (2004)
16	Northeastern Colombia	Vargas et al. (2004)
17	Northeastern Italy	Bianco et al. (2005)
18	Southern Sicily, Italy	Giampiccolo et al. (2006)
19	Asama volcano, Japan	Yamamoto and Sato (2010)
20	Lithosphere and upper mantle	Lee et al. (2003), Lee et al. (2006)
21	Lower mantle (> 670 km depth)	Lee et al. (2003), Lee et al. (2006)
22	Mars	Lognonné et al. (2020)
23	Mars	Menina et al. (2021)
24	Moon	Blanchette-Guertin et al. (2012) Gillet et al. (2017)